

# Mapping early stage of myelin degradation at nanoscale resolution

Nicola Poccia<sup>1,2</sup>, Gaetano Campi<sup>3</sup>, Alessandro Ricci<sup>4,2</sup>, Alessandra S. Caporale<sup>2</sup>,  
Emanuela Di Cola<sup>5</sup>, Thomas A. Hawkins<sup>6</sup>, Antonio Bianconi<sup>2,3</sup>

<sup>1</sup>*MESA+ Institute for Nanotechnology, University of Twente, P. O. Box 217, 7500AE Enschede, The Netherlands.*

<sup>2</sup>*RICMASS Rome International Center for Materials Science Superstripes, via dei Sabelli 119A, 00185 Roma, Italy.*

<sup>3</sup>*Institute of Crystallography, CNR, via Salaria Km 29.300, 00015 Monterotondo Roma, Italy.*

<sup>4</sup>*Deutsches Elektronen-Synchrotron DESY, Notkestraße 85, D-22607 Hamburg, Germany.*

<sup>5</sup>*European Synchrotron Radiation Facility, B. P. 220, F-38043 Grenoble Cedex, France,*

<sup>6</sup>*Department of Cell and Developmental Biology, UCL, Gower Street, WC1E 6BT London, UK.*

## 1. Abstract

To provide insight into the early process of degradation often occurring in severely debilitating diseases with myelin pathology an increased level of spatial structural resolution is needed to bear in the biological realm. Although many observations have connected changes in the periodicity of myelin with illness, few information exist about the microscopic process in the early period of damage of the nerve and how these changes time percolate in space. Here we fill this gap by using first, a short time scale for data collection of scanning micro X-ray diffraction microscopy and second, methods of statistical physics for the analysis of time evolution of this non-invasive local structure experimental approach. We have mapped the time evolution of the fluctuations in myelin period in the degradation nerve process in a freshly extracted sciatic nerve of *Xenopus laevis* with a spatial resolution of 1  $\mu\text{m}$ . We identify the first stage of myelin degradation with the period evolving through a bimodal distribution with a spatial phase separation, and evidence that the orientation of axons in the fresh sample show fractal fluctuations that are reduced with aging.

**Keywords:** *Xenopus*, myelin, lattice fluctuations, imaging degradation, scanning micro X-ray diffraction

**Corresponding author:** Antonio Bianconi. Email: [antonio.bianconi@ricmass.eu](mailto:antonio.bianconi@ricmass.eu)

## 2. Introduction

Myelin is a multilamellar membrane surrounding neuronal axons of both peripheral and central nervous system (respectively, PNS and CNS). A comprehensive understanding of myelin structure-function relation is needed because it is fundamental for normal nervous system function. This is highlighted by the often severely debilitating diseases with myelin pathology such as Multiple Sclerosis [MS: 1] and Charcot Marie Tooth disease [2]. Structural studies of myelin often use the sciatic nerve as representative of the PNS [3] and optic nerves or tracts as representative of the CNS [4].

Many decades of research into the structure-function relationship of myelin have led to the understanding that saltatory conduction by a myelinated axon is mediated by decreased capacitance and increased electrical resistance of the internodal axonal membrane together with a clustering of channels at nodes of Ranvier [5]. These two criteria permit the current to saltate (jump) along the nodes of a myelinated axon. How the biochemical componentry and its arrangement into serial enwrappings of the sheath membrane of myelinating cells mediate the required changes to the electrochemical properties of the system is still not completely elucidated. It has been studied with different approaches such as transmission electron microscopy (TEM) [6], small angle X-ray diffraction [7], coherent Anti-Stokes Raman scattering microscopy [8] spectro-microscopy [9], soft X-ray tomography [10]. From a structural point of view, X ray diffraction (XRD) is widely used to characterize biological tissues and processes [11-18] since it is particularly well suited to study myelin because of its quasi-periodic structure. X-ray diffraction of myelinated axons has attracted interest in the course of the years [19-26].

Indeed, it has been used to get info about various anomalies during nerve degeneration in certain pathologies, resulting e.g. in changes in period and membrane packing [27]. Myelin sheath structural modifications due to the gene encoding mutations, e.g. of the main adhesive P0 glycoprotein, have been revealed using XRD by Avila *et al* [4].

Anyway, conventional XRD has a strong limitation since it provides insight only into the average concentration and molecular structure of the myelin. But myelin is, from a morphological point of view, a very heterogeneous tissue: this makes quite difficult to model its structural features with the conventional experimental approaches, requiring high spatial resolution probes to map spatial changes of structure. Between the mentioned methods, electron microscopy approach (e.g. TEM) can be a local, highly spatially resolved probe, but it is invasive due to sample fixation and dehydration artifacts. Advances in focusing synchrotron beam have allowed to develop the non invasive scanning x-ray diffraction that allows a probe of both the k-space and real space, to visualize the spatial fluctuation of the order of the stacks of myelin membrane stack. Up to now

only low spatial resolution,  $50 \times 50 \mu\text{m}^2$ , mapping of the variations of the structure of myelin sheaths in brain has been achieved. Jensen et al. [10] using small angle x-ray scattering have mapped the concentration and periodicity of the myelin sheaths in a rat brain, looking for correlations between neurofilaments changes and neurodegenerative diseases [28]. Using a similar low resolution ( $50 \times 50 \mu\text{m}^2$ ) De Felici et al. [29] probed a total of 20 different locations in white matter myelin of differently aged subjects, to determine statistical variations of the sizes of the cytoplasm and extracellular regions as well as the thickness of the hydrophilic polar heads and hydrophobic tails in the lipid bilayer. It has already been used to provide unique information on complex functional materials in different research fields ranging from material science, e.g. showing that a loss in the optimum inhomogeneity of the material plays a crucial role in its functional properties [30,32,33], to biomedicine, e.g. monitoring the bone tissue mineralization process [34,35,36].

Here we report the the time evolution of spatial fluctuations of the structure of myelin lamellae at thousands of discrete locations in a freshly extracted *Xenopus* sciatic nerve using a short time scale for data collection. The short time collection data of scanning micro X-ray diffraction ( $S_{\mu}\text{XRD}$ ) microscopy has been reached by using bright synchrotron radiation joined to active X-ray focusing optics and the use of a precise microgoniometer. We have applied statistical physics methods to probe the structural statistical fluctuations of myelin nanoscale order. We have focused our interest on the time variation in the early stage of myelin degradation in a nerve cultured for 18 hours following extraction. Statistical analysis of our measurements describe that: a) the myelin structure periodicity spatial distribution becomes bimodal showing that myelin does not get disordered at the first stage of degradation but myelin assumes a well defined conformation in the first stage of degradation; b) we observe a spatial phase separation between native and degraded conformations; c) the distribution of the orientational fluctuations of the axons in the sciatic nerve shows a fractal probability distribution of large angle fluctuations in the native fresh sample while the orientation distribution becomes randomly distribute with a Gaussian shape in the degraded nerve after 18h culture.

### **3. Materials and Methods**

Two adult female frogs (*Xenopus laevis*; 12 cm length, 180-200g *Xenopus* express, France) were housed and euthanased at the Grenoble Institute of Neurosciences with the kind cooperation of Dr Andre Popov. The animal experimental protocol was approved by the local committee of the Grenoble Institute of Neurosciences. The frogs were individually transferred in water to a separate room for euthanasia which was carried out using a terminal dose of tricaine (MS222) by immersion followed by decapitation. Terminal anaesthesia was confirmed by the absence of reflexes. The sciatic nerve tissue was extracted immediately following decapitation. After dissection, the sciatic

nerves were equilibrated in culture medium at pH 7.3 for at least 3 hours at room temperature. The culture medium was a normal Ringer's solution, containing 115 mM NaCl, 2.9 mM KCl, 1.8 mM CaCl<sub>2</sub>, 5 mM HEPES (4-(2-hydroxyethyl)-1-piperazineethanesulfonic acid). Following equilibration, one of the freshly extracted nerves (henceforth fresh) was immediately placed in a thin-walled quartz capillary, sealed with wax and mounted on the sample holder for the S $\mu$ XRD imaging measurements. The other nerve (henceforth the *unfresh* nerve) was left in the culture medium for another 15 hours, and finally mounted on the sample holder to perform  $\mu$ XRD. The nerves were fixed by immersion for 24 hours in a solution of 2% paraformaldehyde, 2% glutaraldehyde in 0.1 M sodium cacodylate buffer (pH 7.3), rinsed in 0.1 M sodium cacodylate. Following transport to UCL, London, they were post-fixed in cacodylate-buffered 1% (w/v) osmium tetroxide, dehydrated through an ethanol series and embedded in Agar 100 resin (Agar Scientific). Ultrathin sections (80-100nm) were contrasted with lead citrate, examined and photographed using a JEOL 1010 electron microscope and Gatan digital camera.

The experimental apparatus for Scanning Micro X-Ray Diffraction (S $\mu$ XRD), shown schematically in **Figure 1a**, is located at the European Synchrotron Radiation Facility (ESRF). The source of the synchrotron radiation beam is a 18 mm period in-vacuum undulator, providing 12–13-keV X-rays to crystal optics. The beam is first monochromatized (X-ray energy 12.4 keV) by a liquid nitrogen cooled Si-111 double monochromator; then is focused by a Kirkpatrick–Baez (KB) mirror system to give a flux of 10<sup>10</sup> counts/second on 1x1  $\mu$ m area. The sample holder hosts the capillary-mounted nerve with the longitudinal axis laying on the vertical x-axis, and allows y-z translation stages.

A Fast Readout Low Noise (FReLoN) camera (2048 x 2048 pixel, 24 x 24  $\mu$ m<sup>2</sup> pixel size) is placed at a distance of 820 mm from the sample to collect the 2-D diffraction patterns in transmission. Detector characteristics and specimen-to-film distance were established by recording diffraction patterns from a standard consisting of silver behenate powder (AgC<sub>22</sub>H<sub>43</sub>O<sub>2</sub>), which has a fundamental spacing of  $d_{001}$ =58.38 Å [37, 38]. The exposure time was 300 ms for scattering measurements. **Figure 1b** shows the 2-D diffraction pattern of the organized myelin membrane, as recorded by the areal detector showing four pairs of diametrically opposed arcs. The large spot in the middle of the image is due to the diffuse scattering from the beam stopper.

Through the use of FIT2D (Andy Hammersley, ESRF, Grenoble, France), the diffraction intensity within the rings may be integrated both azimuthally and radially, and the 1-D X-ray patterns are easily extrapolated.

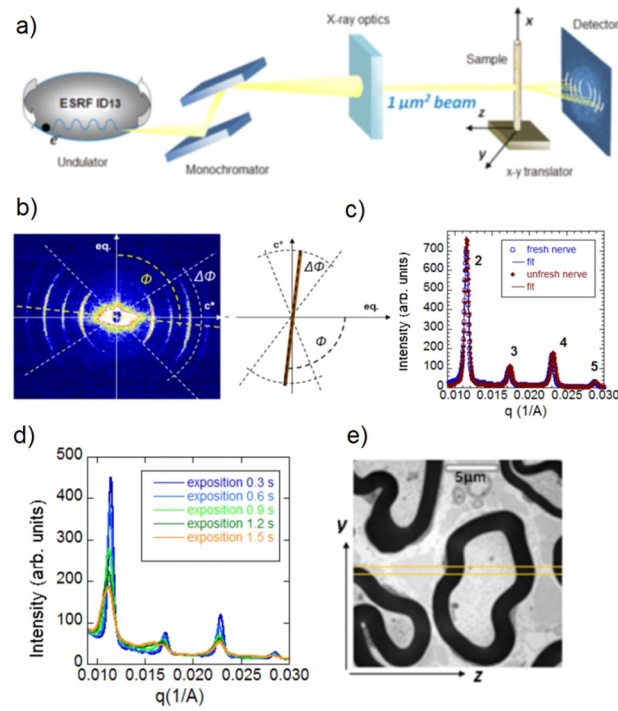


**Figure 1** (a) The experimental apparatus is located at the European Synchrotron Radiation Facility (ESRF) and features an electron undulator providing 12.4 keV X-rays to crystal optics. The sample holder houses a 1 mm-diameter quartz capillary containing the nerve and the culture medium. The x-y translator allows the sample to move in both horizontal and vertical directions with a sampling step of 5  $\mu\text{m}$  within a selected area. The X-rays scattered by the sample are recorded by a FReLoN detector. (b) The 2D diffraction pattern shows 4 concentric rings, with symmetrical arcs of high intensity with respect to the equatorial axis, (eq.). The  $c^*$  axis overlaps with the axis of symmetry of the ideal axon-cylinder. The arcs are displaced around the direction indicated by the azimuthal angle  $\Phi$ , counted from the eq. axis, and have an amplitude of  $\Delta\Phi$ . The tilting of myelin reveals an angular dispersion of the axons in the way they are arranged in the nerve. (c) Observed intensity distributions of the sciatic nerve bathed in normal Ringer's solution at pH 7.3 and exposed to X-rays after 3 hours (fresh nerve, empty circles) and 18 hours (unfresh nerve, filled dots) from the extraction, after background subtraction and normalization with respect to the impinging beam. The intensity (in arbitrary units) is plotted against the reciprocal distance ( $\text{\AA}^{-1}$ ). The unfresh nerve produces a diffraction pattern with a slightly higher intensity (see the reflection  $h = 2$ ). (d) Patterns of the fresh sciatic nerve under physiological conditions (pH 7.3, 115 mM NaCl), exposed to the impinging beam at a sample-to-film distance of 820 mm, for progressively increasing time intervals. The intensity is given in arbitrary units, and plotted as a function of the reciprocal distance  $\text{\AA}^{-1}$ . Notice the substantial alteration of the peak shape and broadening especially for the first two reflections, with increasing exposition time. (e) A typical TEM micrograph of an ultrathin section of the sciatic nerve, where myelinated axons of various diameters are visible. The superimposed yellow lines represent the impinging X-ray beam of 1  $\mu\text{m}$  width, 6000x magnification, scale bar 5  $\mu\text{m}$ . The image shows no evidence of degradation after the exposure of 0.3 second.

A typical X-ray diffraction (XRD) pattern, radially integrated, is depicted in **Figure 1c**; it shows the Bragg diffraction orders  $h = 2, 3, 4, 5$ . corresponding to the concentric rings of Fig. 1b produced by the ordered structure of the myelin multilayer. The XRD diffraction patterns were normalized with respect to the intensity of the impinging beam  $I_0$ . Background scattering from the empty capillary was measured and subtracted, and the resulting peaks above background were fit by Gaussians (Fig. 1c). The areas of the peaks or integral areas  $I(h)$  and the integral widths  $w(h)$  were used to calculate the structure amplitudes for each reflection of order  $h$ , according to  $|F(h)| = \sqrt{hI_{obs}(h)}$ .

These structure factors were employed in a Fourier synthesis to extract the Electron Density Distribution (EDD) of the myelin multilayer, according to  $\rho(r) = F(0)/d + (2/d) \sum_{h_{min}}^{h_{max}} \pm F(h/d) \cos(2\pi rh/d)$ . where the phases were taken from literature [39, 40]. From the EED profile the widths of the inter-membrane spaces at the cytoplasmic (*cyt*) and extracellular (*ext*) appositions and the thickness of the lipid bilayer (lipid polar groups, *lpg*) were obtained. These structural parameters are defined as the distances between the middles of the head group layers across the intermembrane (extracellular and cytoplasmic) spaces and within a single bilayer [41]. The period *d* or radial repeating unit of the myelin sheath, that is the center-to-center layer distance within the radial packing of myelin, includes two lipid polar bilayers that belong to the cellular membrane of the myelin generating Schwann cell, the cytoplasm comprised between these bilayers, and the extracellular space included in the sheath during the process of myelination:  $d = ext + cyt + 2lpg$  [42].

Our investigation through S $\mu$ XRD imaging was aimed to quantify the early changes in the ultrastructure of myelin in the degradation of a fresh nervous tissue, therefore it was of fundamental importance to minimize any possibility of damage of the nerve. In dependence on the radiation dose, cells may be undamaged, they can be damaged either repairing properly the damage or operating abnormally, and they can even die as a result of the damage. The data acquisition is thus preceded by an estimation of the radiation damage, to test the actual tissue damage due to the X-ray impinging beam that has a fixed energy. This leads to the estimate of the most suitable exposition time which ensures the best signal with the least alteration of the sample. As you can see in **Figure 1d**, the diffraction pattern is abnormal from an exposure time of 0.9 s, with a sensible broadening of the peaks, and a noisier profile. The ionization and excitation of electrons, and eventually the subsequent emission of X-rays when the electrons from the outer shells fill the holes, determines an alteration of the diffraction pattern: well-defined peaks broaden, meaning that the crystalline order of the myelin sheath has been dismantled. We decided to use an exposure time of 300 ms which does not sacrifice the sensitivity, minimizing the radiation damage at the same time.

From the Transmission Electron Microscopy (*TEM*) micrographs (see **Figure 1e**) of the specimens it is possible to infer that the X-ray impinging beam crosses each step a bundle of approximately 50 axons. TEM demonstrated that the culture conditions in the small quartz capillary did not appreciably affect the morphology of myelin in the nerves, and provided a direct comparison between the irradiated nerves and the samples kept away from the X-ray beam, showing that the X-ray exposure of 300 ms employed did not alter visibly the structure of myelin.

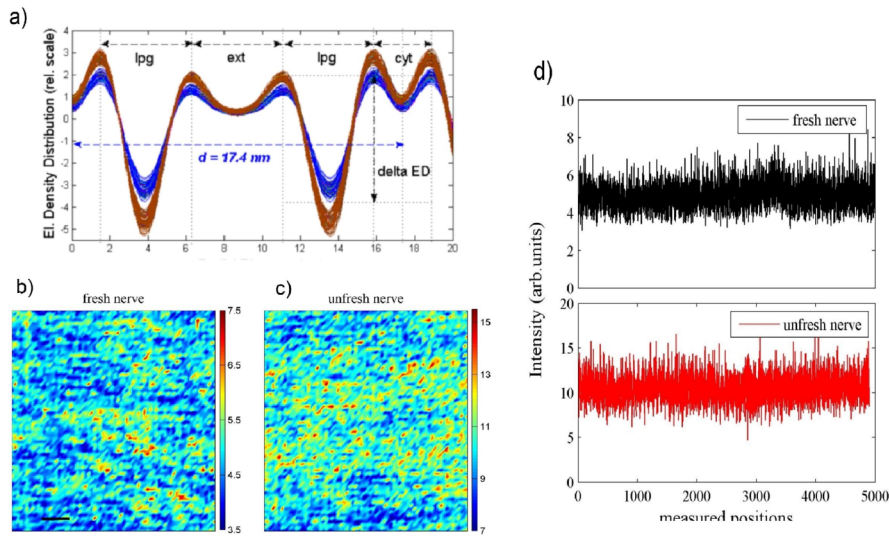


**Figure 2 (a)** The electron density profiles computed for each pixel of a central row in the selected meshes for fresh nerve, (empty blue circles) and unfresh nerve, (brown dots). The curve presents troughs and maxima, with a period of  $d = 17.4$  nm for the fresh sample. **(b, c)** Maps of the integral intensity of X-ray pattern in a selected ( $300 \times 300 \mu\text{m}$ ) central zone for **(b)** fresh and **(c)** unfresh nerve extracted after 3 and 18 hours respectively; the integral intensity in each pxel is the area of the X-ray pattern after background subtraction and normalization for the incident flux. The intensity behavior, corresponding to the myelin amount in the sample, point by point, is shown **(d)** for both fresh and unfresh nerve. We observe the normal behavior of the integral intensity fluctuations, ensuring us that the selected zone is not affected by artifacts, such as significant differences in myelin concentration due, e.g. to the cylindrical geometry of the sample.

#### 4. Results and discussion

The samples were measured in region of interests (ROI) made of 20302 pixels (corresponding to a surface of  $0.505 \text{ mm}^2$ ) with a total acquisition time of the scanning procedure of approximately 1 h 40 mins. In each pixel the ordered multilayer structure of the myelin sheath within the exposed sciatic nerve produced diffraction pattern showed in Fig.1b.

The amplitude, width and position of the reflection peaks, permitted the derivation of the electron density distribution (EDD) as previously described in sec .3. Figure 2a represents the electron density profiles of the myelin sheaths computed in a radial direction for each pixel of a central row of the selected meshes in the fresh and unfresh samples. The zero of the radial axis corresponds to the internal rings of Schwann cell cytoplasm that separate the axons from the myelin sheath. The differences between two adjacent maxima in the EDD, indicated by horizontal arrows in **Figure 2a**, provide the following quantities: i) the thickness of the lipid polar layer (*lpg*), ii) the width of the extracellular space (*ext*) and iii) the width of the cytoplasmic space (*cyt*). The vertical arrow in Figure 2a indicates the difference between the electron density of the intracellular space and extracellular space at the *lpg* apposition (*delta ED*). The lipid tails (corresponding to the middle of the *lpg* region) have the lowest electron density because of the high hydrogen concentration [28].

The extrapolation of EDD and the computation of sizes of coherent scattering domains and barriers of density were performed for each pixel of the ROIs using a customized in-house developed code written in MatLab (Mathworks, Natick, MA). The extracted described quantities *ext*, *cyt*, *lpg*, *d*, *delta ED* were subjected to statistical analysis considering the EDDs of two regions with the same number of pixels within the ROIs of the fresh and unfresh samples. These regions were taken from the middle of each ROI, in order to consider the central part of the nerve where it is thickest and most parallel to the capillary wall. Here the amount of myelin has a normal behavior, as we can observe in **Figure 2b**, **2c** and **2d**. Maps reporting the integral intensity of spectra in the measured zones of both *fresh* and *unfresh* nerve are shown in Fig. 2c and 2d respectively. The integral intensity in each pixel is the area of the whole X-ray pattern after background subtraction and normalization for the incident flux. The intensity behavior, corresponding to the myelin amount in the sample, point by point, is shown Fig. 2d for both fresh and unfresh nerve. We observe the normal behavior of the integral intensity fluctuations, ensuring us that the selected zone is not affected by artifacts, such as significant differences in myelin concentration due, e.g. to the cylindrical geometry of the sample.

The native period of multilamellar myelin is observed near physiological ionic strength at neutral, slight alkaline pH [41, 42]. The color-maps shown in **Figure. 3a**, **3b** represent the periodicity *d* of the fresh and unfresh samples at pH 7.3 and 115mM NaCl, estimated from the electron density profile as the sum of the *cyt*, *ext*, double *lpg* widths for the selected 0.300 x 0.300 mm<sup>2</sup> ROI. The myelin periodicity of the fresh nerve is  $d = (173.6 \pm 0.3) \text{ \AA}$ , in agreement with Luo et al. [43]. The map related to the fresh nerve in Fig. 3a presents a homogeneous distribution of yellow-orange spots. Our key observation is that the map of the unfresh sample (see Fig. 3b) shows a phase separation between the yellow-orange and a blue macro region, corresponding respectively to a higher and a lower value of *d*. The probability density functions of the myelin periodicity in Fig. 3c is a unimodal Gaussian lineshape for the fresh nerve, and becomes bimodal in the unfresh nerve. The presence of the two Gaussians indicates that the early state of myelin degradation is a transition to a slightly different structural conformation characterized by a shorter periodicity, conserving a similar width of the distribution.

The two mean values of *d* and the full width half maximum (FWHM) of the unimodal and the two contributes of the bimodal distributions are shown in Table. 1. The value of *d* varies only within a range of 2 Å in the observed transition; in fact the relative standard deviation (RSD) is inferior to 0.2% for both samples. The main contribution to the decreased periodicity is due to a compression of the myelin cytosol layer. In fact, mean value of the extracellular space width does not change appreciably, and the thickness of the lipid polar groups slightly increases.

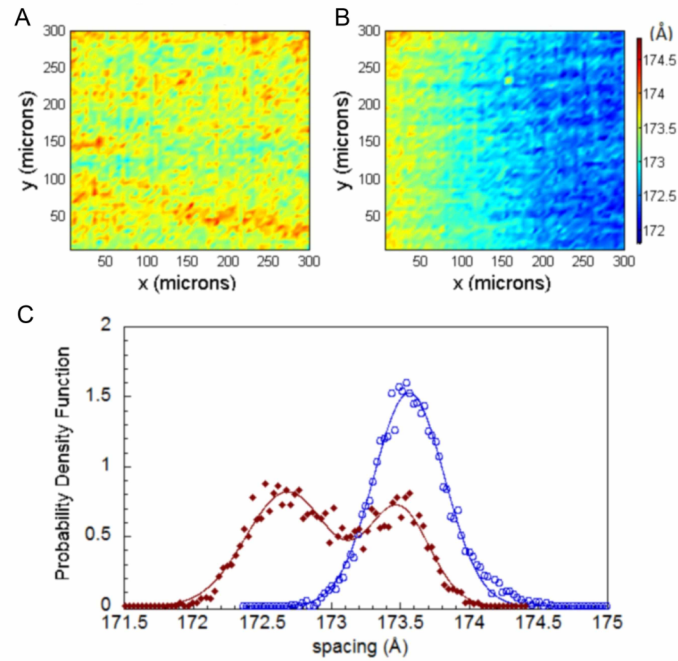


**Figure 3** Colormaps of the computed myelin periodicity in a  $0.300 \times 0.300 \text{ mm}^2$  ROI of the (a) fresh and (b) unfresh *Xenopus laevis* sciatic nerves in the capillary. The figures show a matrix of  $60 \times 60$  pixels, of size  $5 \mu\text{m}$ . The pixel color is related to the value of periodicity estimated from the electron density profile. The map in (a) shows a prevalence of yellow-orange spots, distributed fairly evenly within the ROI, while the map in (b) presents two distinct macro-regions of hot and cold colors. (c) Probability density function of the periodicity, given by the sum of the *cyt*, *ext*, double *lpg* widths (fresh nerve, empty blue circles; unfresh nerve, brown dots). This distribution is unimodal for the fresh sample and bimodal for the unfresh one, with a total wider FWHM. The periodicity varies within a range of about  $2 \text{ \AA}$  in the transition from the living to the dying state.

**Figure 4a** shows a  $0.4 \text{ \AA}$  shift in the mean value of the cytoplasmic space width during the 15 hours between sample recordings. The mean value of the extracellular space width does not change appreciably, and the thickness of the lipid polar groups slightly increases. A reduction of the FWHM generally occurs in the distributions of widths of the unfresh nerve, compared to the fresh one, and it is compelling for the extracellular space width (**Fig 4b, 4c**) in agreement with the results of Luo et al.[43], who performed XRD (with conventional X-ray equipment) using a *Xenopus laevis* sciatic nerve at pH 7.3 and physiological ionic strength. The width of the extracellular domain and the thickness of the lipid polar groups both fit with them within the experimental error, but the width of the cytoplasmic space is about  $4 \text{ \AA}$  less than those observed by Luo et al.  $\text{cyt} = 34 \text{ \AA}$  [43]. We should consider that these values may be influenced by the experimental setup (the X-ray source, the culture medium, the duration of the experiment, the temperature of the room), or by an intrinsic variability within the *Xenopus* species (age, size, weight of the exposed frogs).

Luo et al. used the  $\text{CuK}_\alpha$  radiation from a fine-line source, a normal Ringer's solution, and adult female frogs, exposed for interval times ranging from 15 mins to  $1\text{h}^3$  while in our synchrotron radiation experiment each XRD frame was collected in 0.3 s. The main differences are therefore the X-ray source and the exposition time. The transition that occurs in the 15 hrs between sample

recordings gives an increment of delta ED between the intracellular and extracellular space that translates in a higher mean value in the probability density function shown in **Fig. 4d**. A possible explanation for this is that the density barrier between the internal and the external environment of the cell increases following an extended culture time.

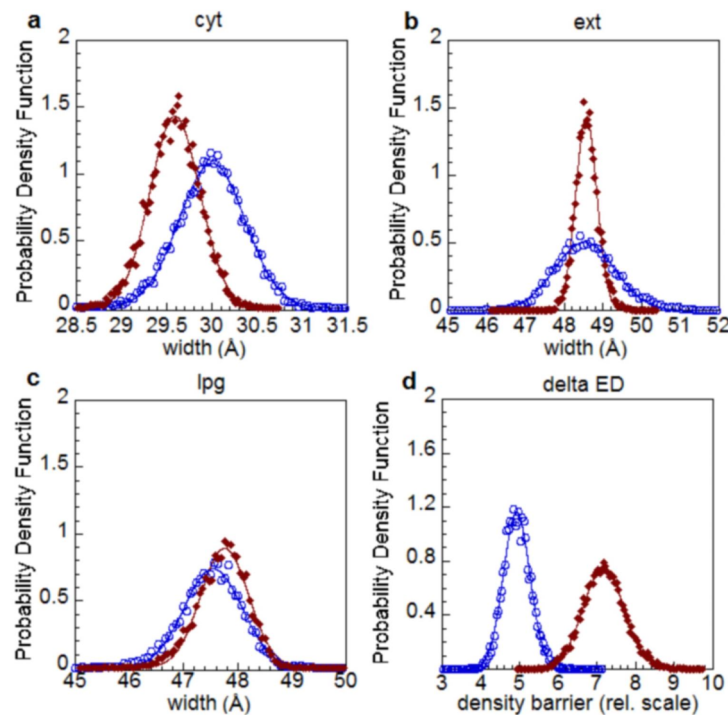


**Figure 4** Probability density functions of the cytoplasmic space - cyt (a), extracellular space - ext (b), lipid polar groups - lpg (c) and the difference of electron density - delta ED - between the inside and outside of the cell at the lpg apposition (d) for the myelin sheath of *Xenopus laevis* sciatic nerve at 3 hours (fresh nerve, empty blue circles) and 18 hours (unfresh nerve, brown dots) after extraction. The markers indicate the experimental values; the continuous lines indicate the Gaussian fit. There is a considerable reduction of the mean value of the cytoplasmic space width (a), while the mean value of the extracellular space width does not change appreciably (b), and the thickness of the lipid polar groups slightly increases (c). A reduction of the FWHM generally occurs comparing the fresh to the unfresh samples, and it is particularly evident for the extracellular space width (b). The distribution of delta ED (d) in the unfresh sample shows a higher mean value.

This putative increase could be because of a reduction of ionic fluctuations across the membrane in the nerve 18 hours from the extraction.

The myelin sheath, generated by multiple phospholipid membranes of the Schwann cell, together with embedded proteins and sterols, is an example of a lyotropic liquid crystal, consisting of organic solid crystals dissolved in a polar solvent that exhibits liquid-crystalline properties [44] in

certain concentration ranges. It presents therefore a partially retained translational and orientational order (typical of the crystal solid) and acquires in part the properties of an isotropic solvent [45]. Through the  $S_{\mu}$ XRD it is possible to map the orientation of the myelin packing within the nerve fiber, and to infer from this the average orientation of the axons producing the diffraction (the axis of which is perpendicular to the direction of myelin packing). Many techniques allow the visualization of isolated axons such as X-ray fluorescence microscopy, atomic force microscopy, and scanning electron microscopy [9], but up to now the variability in the orientation of axons within the nerve has never been quantified. The  $1\mu\text{m}$ -thick sciatic nerve contains several hundreds of axons, many of which are myelinated. The axons will be in many different configurations relative to the overall orientation of the nerve and to the wall of the capillary; however, because the beam passes through several myelinated fibres, the diffraction pattern at each point is an average. The nerve is near to parallel to the capillary wall and thus it is reasonable to assume that the pattern at each imaging locus is equivalent to a readout of a myelin sheath that represents the general trend of sheath orientation in that area of the nerve. Thus, using this method we can gain a picture of general sheath orientational changes along and across the nerve. Although this is limited to a general picture of the nerve in a quasi-natural state it is interesting to examine if an analysis of variation in this metric is feasible. Thus, we analyzed the preferential azimuthal angle of each data point.

The amplitude of the rings,  $\Delta\Phi$ , of the angle  $\Phi$ , spanned from the equatorial axis, represents the spread in the orientation of the stacking of the myelin lamellae. The  $c^*$  axis overlaps with the axis of symmetry of the ideal myelinated axon-cylinder. These quantities, were computed through an azimuthal integration (at fixed  $q$  range) of the diffraction intensity of the rings over each of the 20302 diffraction frames. The tilting of the myelin packing, represented by  $\Delta\Phi$ , reveals an angular dispersion trend in the orientation of the myelinated axons in the nerve. The azimuthal dispersion may be easily visualized through the colormaps depicted in **Figure 5**.

The maps in **Figs. 5a, 5b** show a total orientational spread of at least  $30^\circ$ , meaning that the bundles of axons are not perfectly parallel to each other. **Figure 5c** shows the differences between 3hr and 18hr samples in the PDF distribution of the orientations  $\Delta\Phi$ . By comparing the PDF, we notice a distribution with a fatter tail for the fresh sample compared to the unfresh one.

Fitting the PDF with a log normal distribution  $y(x) = \frac{\exp\{-(\ln x - \mu)^2 / 2\sigma^2\}}{\sqrt{2\pi\sigma^2 x}}$ , we obtain a location

parameter  $\mu = 3.4437$ , a scale parameter  $\sigma = 0.2494$ , and a mean value  $\Delta\bar{\Phi}_f = e^{\mu + \sigma^2/2} = 32^\circ.3$ .

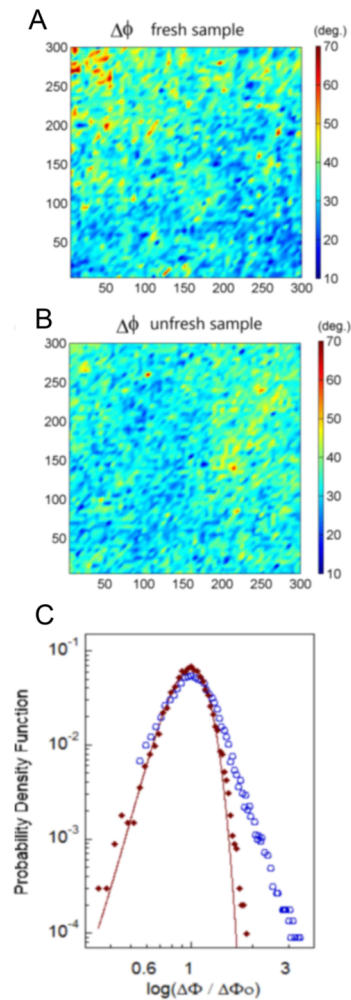


**Figure 5** Maps of axons orientational fluctuations,  $\Delta\Phi$ , in an area of  $0.300 \times 0.300 \text{ mm}^2$  of the (a) fresh and (b) unfresh (c) Probability density function of the  $\Delta\Phi$  tilting angle for the fresh (empty blue circles) and unfresh (brown dots) samples. The distributions show that the crystallites, represented by the myelinated axons within the nerve trunk in the capillary, have a preferred orientation (axons parallel to the capillary walls), represented by the mean value  $100^\circ$ , with a tilting angle of about  $10^\circ$ . The log-log plot is useful to visualize the fat tail of the probability density function of fluctuations for the fresh sample compared to the unfresh one.

The distribution of  $\Delta\Phi$  for the 18hr sample is simply Gaussian instead, with a mean value  $\Delta\Phi_u = 32^\circ.8$ . In order to visualize clearly the difference between the two tales the  $\log(PDF)\text{-}\log(\Delta\Phi)$  plot is considered (Fig. 5c). This indicates an interesting change occurring following longer culture times. This result describes changes in the spatial fluctuations taking place during death of myelinating glia and subsequent degradation of myelin in the nerve. Particularly interesting is the difference between the samples at higher log values. The distribution of the orientational fluctuations of the fibers in the sciatic nerve shows a higher probability of large angle fluctuations in the fresh sample than in a sample after 18h culture. The longer fat tail indicates a tendency of the system towards a fractal spatial organization [46,47,48,49] in the native nerve which becomes a normal Gaussian distribution in the early stage of myelin degradation. The change occurring

between 3hrs and 18hrs due to degradation shows that the difference in the tails of the distributions might support that the transition from a living state to a dying/degrading one corresponds to the end of more subtle fluctuations in sheath orientation.

## 5. Conclusions

In this work we demonstrate the feasibility of applying  $S_{\mu}$ XRD for non invasive imaging of time evolution of living PNS myelin. This technique allowed us to map the main quantities (*ext*, *cyt*, *lpg*, *d*, *delta ED*) in the ultra-structure of freshly extracted myelinated peripheral nerve, with high spatial resolution of 1  $\mu$ m. The evolution of these quantities with tissue aging and degradation in prolonged culture of the nerve is characterized by the following main evidences: i) a crossover from quite constant unimodal to bimodal distribution of periodicity, *d*; ii) a spatial phase separation between native and degraded conformations; iii) a slight, but significant decrease in the width of the cytoplasmic space, *cyt*; iii) the distribution of the orientational fluctuations of the axons in the sciatic nerve shows a like-fractal probability distribution of large angle fluctuations in the native fresh sample while the orientation distribution becomes randomly distribute with a Gaussian shape in the degraded nerve after 18h culture. TEM observations suggest that the transition we see is not derived from obvious morphological changes. It is possible that this transition represents an early step in the degradation of the myelin sheath undetectable by microscopic observation. The investigation of time evolution of spatial fluctuations in myelin structure by  $S_{\mu}$ XRD opens perspectives to investigate putative structural correlations with functionality, as proposed elsewhere [50, 51], particularly the mode by which the structure of myelin interacts with the flux of ions during the propagation of the axon potential. The present findings on the interplay between order and disorder in a complex heterogeneous and fluctuating system such as myelin show that the short time scale for data collection joint with a statistical analysis of  $S_{\mu}$ XRD measurements open fantastic perspectives to unveil the time evolution of spatial order and disorder in biological cell.

**6.Acknowledgements.** The authors thank the ESRF for financial assistance and the ID13 group for support during the experiment and the kind cooperation of Dr. Andre Popov. N.P. acknowledge the Marie Curie Intra European Fellowship for financial support.

**7. Disclosure.** The authors declare to have no conflict of interest. This does not alter our adherence to all the PLOS ONE policies on sharing data and materials

<b>Table 1</b> Statistical analysis of the quantities computed from the electron density profiles			
	$\mu$ (Å)	<i>FWHM</i> (Å)	<i>RSD</i> (%) <sup>b</sup>
Fresh sample <sup>a</sup>			
<b>cyt</b>	30.00	0.8431	1.22
<b>lpg</b>	47.54	1.230	1.13
<b>ext</b>	48.52	1.790	1.60
<b>per</b>	173.6	0.5895	0.150
<b>delta ED</b>	4.922	0.7869	6.95
Unfresh sample <sup>a</sup>			
<b>cyt</b>	29.59	0.6372	0.940
<b>lpg</b>	47.76	1.019	0.930
<b>ext</b>	48.57	0.6303	0.560
<b>per</b>	172.7/173	0.6962/0.51	0.180/0.1
	.5	56	30
<b>delta ED</b>	7.165	1.2122	7.36

**Table 1**<sup>a</sup> The two *Xenopus laevis* sciatic nerves were extracted and placed in normal Ringer's solution at pH 7.3 and 115 mM NaCl. The fresh sample was inserted in the capillary with the culture medium to perform SMXRD after a resting period of 3 hours, while the unfresh sample was exposed to X-rays after a resting period of 18 hours.<sup>b</sup> The relative standard deviation (RSD) was computed as the ratio between the standard deviation  $\sigma$  (not indicated in the table) and the mean value  $\mu$ .

## 8. References

1. Dutta R, Trapp BD. Pathogenesis of axonal and neuronal damage in multiple sclerosis. (2007) *Neurology* **68**: S22-S31 PMID: 17548565
2. Valentijn LJ, Baas F, Wolterman RA, Hoodgendijk, van den Bosch NHA et al. (1992) Identical point mutations of PMP-22 in Trembler-J mouse and Charcot-Marie-Tooth disease type 1A. *Nat. Gen.* **2**: 288-291 PMID: 1303281
3. Luo XY, Cerullo J, Dawli T, Priest C, Haddadin Z et al. (2008). *J. Struct. Bio.* **162**: 170-183.
4. Avila RL, Inouye H, Baek RC, Yin X, Trapp BD. Structure and Stability of Internodal Myelin in Mouse Models of Hereditary Neuropathy. *J. Neuropathol. Exp. Neurol.* 2005) **64**: 976-990. doi:10.1016/j.jsb.2007.10.012
5. Hartline DK, and Colman DR. (2007) Rapid Conduction and the Evolution of Giant Axons and Myelinated Fibers. *Curr Biol.* **17**: R29–R35. <http://www.sciencedirect.com/science/article/pii/S0960982206025231>

6. Finean JB. (1960) Electron microscope and X-ray diffraction studies on the effect of dehydration on the structure of nerve myelin. *J. Biophysic. And Biochem. Cytol.* **8**: 13-29. PMID: PMC2224905
7. Avila RL, Tevlin BR, Lees JPB, Inouye H, Kirschner DA. (2007) Myelin Structure and Composition in Zebrafish. *Neurochem. Res.* **32**: 197-209. <http://www.ncbi.nlm.nih.gov/pubmed/16951904>
8. Wang H, Fu Y, Zickmund P, Shi R, Cheng JX (2005) Coherent Anti-Stokes Raman Scattering Imaging of Axonal Myelin in Live Spinal Tissues. *Biophys. J.* **89**: 581–591. <http://www.ncbi.nlm.nih.gov/pubmed/15834003>
9. Ducic T, Quintes S, Nave KA, Susini J, Rak M et al. (2011) Structure and composition of myelinated axons: a multimodal synchrotron spectro-microscopy study *J Struct. Biol.* **173**, 202-212. DOI: 10.1016/j.jsb.2010.10.001
10. Jensen TH, Bech M, Bunk O, Menzel A, Bouchet A et al. (2011) Molecular X-ray computed tomography of myelin in a rat brain. *NeuroImage.* **57**: 124-129. doi: 10.1016/j.neuroimage.2011.04.013
11. Schmitt FO, Bear RS & Clark GL (1935) X-ray diffraction studies on nerve. *Radiology*, **25**: 131-151.
12. Yamada H (1959) X-ray Diffraction and Electron Microscopic Studies of the Myelin Sheath. *Pathology International* **9**: 255–265. DOI: 10.1111/j.1440-1827.1959.tb00317.x
13. Akers CK and Parsons DF (1970) X-Ray Diffraction of Myelin Membrane, *Biophysical Journal*, **10**: 116-136. <http://www.ncbi.nlm.nih.gov/pmc/articles/PMC1367725/>
14. Hybl A, (1977) “Paracrystalline Nature of Myelin” *J. Appl. Cryst.* **10**: 141-146. doi:10.1107/S0021889877013132
15. Schliess F, Stoffel W (1991) “Evolution of the myelin integral membrane proteins of the central nervous system” *Biological Chemistry Hoppe-Seyler* **372**: 865-874. DOI: [10.1515/bchm3.1991.372.2.865](https://doi.org/10.1515/bchm3.1991.372.2.865),
16. Padrón R, Mateu L and Kirschner DA, (1979) “X-ray diffraction study of the kinetics of myelin lattice swelling. Effect of divalent cations” *Biophys. J.*, **28**: 231-239. PMID: PMC1328627 [http://ac.els-cdn.com/S0006349579851735/1-s2.0-S0006349579851735-main.pdf?\\_tid=94650c6c-6345-11e3-92e6-00000aab0f6c&acdnat=1386863804\\_4a096a9e6a41b7992cb11e74aa899635](http://ac.els-cdn.com/S0006349579851735/1-s2.0-S0006349579851735-main.pdf?_tid=94650c6c-6345-11e3-92e6-00000aab0f6c&acdnat=1386863804_4a096a9e6a41b7992cb11e74aa899635)
17. Changizi V, Arab Kheradmand A, and Oghabian MA. (2008) Application of small-angle X-ray scattering for differentiation among breast tumors *J. Med. Phys.* **33**: 19–23. doi: 10.4103/0971-6203.39420.

18. Ciasca G, Chiarpotto M, Campi G, Bocca B, Rodio M, Pino A, Ricci A et al. (2011) "Reconstitution of aluminium and iron core in horse spleen apoferritin" *J. Nanopart. Res.* **13**: 6149-6155. Doi: 10.1007/s11051-011-0294-2 URL <http://link.springer.com/article/10.1007/s11051-011-0294-2#page-1>
19. Schmitt FO, Bear R S and Palmer K J (1941) "X-ray diffraction studies on the structure of the nerve myelin sheath" *Journal of Cellular and Comparative Physiology* **18**: 31-42. DOI: 10.1002/jcp.1030180105
20. Fernandez-Moran H, and Finean JB (1957) "Electron microscope and low-angle x-ray diffraction studies of the nerve myelin sheath" *The Journal of biophysical and biochemical cytology* **3**: 725-748. PMID: 13475388 <http://www.ncbi.nlm.nih.gov/pmc/articles/PMC2224112/pdf/725.pdf>
21. Schmitt F O, Bear RS, and Clark GL (1935) "X-ray diffraction studies on nerve" *Radiology* **25**: 131-151. <http://pubs.rsna.org/doi/abs/10.1148/25.2.131>
22. Worthington CR, and Blaurock AE (1969) "A low-angle x-ray diffraction study of the swelling behavior of peripheral nerve myelin" *Biochimica et Biophysica Acta (BBA)-Biomembranes* **173**: 427-435. [http://dx.doi.org/10.1016/0005-2736\(69\)90007-8](http://dx.doi.org/10.1016/0005-2736(69)90007-8)
23. Kirschner D A, and Sidman RL (1976) "X-ray diffraction study of myelin structure in immature and mutant mice" *Biochimica et Biophysica Acta (BBA)-Biomembranes* **448**: 73-87. PMID: 971429 URL <http://www.ncbi.nlm.nih.gov/pubmed/971429>
24. Agrawal D, et al. (2009) "Internodal myelination during development quantitated using X-ray diffraction" *Journal of structural biology* **168**: 521-526. doi: 10.1016/j.jsb.2009.06.019
25. Höglund G and Ringertz H (1961) "X-Ray Diffraction Studies on Peripheral Nerve Myelin." *Acta Physiologica Scandinavica* **51**: 290-295. doi: 10.1016/j.jsb.2009.06.019.
26. Kirschner, Daniel A., Allen L. Ganser, and Donald LD Caspar. (1984) "Diffraction studies of molecular organization and membrane interactions in myelin." *Myelin*. Springer US, pp. 51-95.
27. Lampert PW (1965) "Demyelination and remyelination in experimental allergic encephalomyelitis. Further electronmicroscopic observations" *J. Neuropathol. Exp. Neurol.* **24**: 371-85 DOI:10.1097/00005072-196507000-00001
28. Liu Q, et al., (2004) Neurofilament proteins in neurodegenerative diseases. *Cell. Mol. Life Sci.* **61**: 3057-3075. DOI 10.1007/s00018-004-4268-8
29. De Felici M, Felici R, Ferrero C, Tartari A, Gambaccini M et al. (2008) Structural characterization of the human cerebral myelin sheath by small angle x-ray scattering. *Phys Med Biol.* **53**: 5675-5688. doi: 10.1088/0031-9155/53/20/007.

30. Poccia N, Campi G, Fratini M, Ricci A, Saini NL, and Bianconi A. (2011) Spatial inhomogeneity and planar symmetry breaking of the lattice incommensurate supermodulation in the high-temperature superconductor  $\text{Bi}_2\text{Sr}_2\text{CaCu}_2\text{O}_{8+y}$ . *Phys. Rev.B*, **84**: 100504(R).  
<http://prb.aps.org/abstract/PRB/v84/i10/e100504> , DOI: 10.1103/PhysRevB.84.100504
31. Poccia N, Ricci A, Campi G, Fratini M, Puri A, Di Gioacchino D., et al. (2012) Optimum inhomogeneity of local lattice distortions in  $\text{La}_2\text{CuO}_{4+y}$ . *Proc. Natl. Acad. Sci. USA*, **109**: 15685-15690. Doi: [10.1073/pnas.1208492109](https://doi.org/10.1073/pnas.1208492109)
32. Poccia N., Fratini M., Ricci A., et al. (2011) Evolution and control of oxygen order in a cuprate superconductor *Nat Mater.* **10**: 733-736.  
<http://www.nature.com/nmat/journal/v10/n10/full/nmat3088.html> doi:10.1038/nmat3088
33. Campi G, Ricci A, Poccia N, Barba L, Arrighetti G., Burghammer M, et. al. (2013) Scanning micro-x-ray diffraction unveils the distribution of oxygen chain nanoscale puddles in  $\text{YBa}_2\text{Cu}_3\text{O}_{6.33}$ . *Phys. Rev. B*, **87**: 014517 DOI: 10.1103/PhysRevB.87.014517
34. Paris O. (2008) From diffraction to imaging: New avenues in studying hierarchical biological tissues with x-ray microbeams (Review), *Biointerphases*, **3**: FB16.
35. Seidel R, Gourrier A, Burghammer M, Riekel C, Eronimidis JG, Paris O. (2008) Mapping fibre orientation in complex-shaped biological systems with micrometre resolution by scanning X-ray microdiffraction *Micron.* **39**: 198-205.
36. Campi G, Ricci A, Guagliardi A, Giannini C, Lagomarsino S, Cancedda R, Mastrogiacomo M, and Cedola A. (2012) Early stage mineralization in tissue engineering mapped by high resolution X-ray microdiffraction *Acta Biomater.* **8**: 3411. doi: 10.1016/j.actbio.2012.05.034.
37. Blanton TN, Huang TC, Toraya H et al.. (1995) JCPDS International Centre for Diffraction Data round robin study of silver behenate. A possible low-angle X-ray diffraction calibration standard. *J Powder Diffraction* **10**: 91-95.
38. Huang TC, Toraya H, Blanton TN et al. (1993) X-ray-powder diffraction analysis of silver behenate. A possible low-angle diffraction standard. *J Appl Crystallogr* **26**: 180-184.
39. Harker D. (1972) Myelin membrane structure as revealed by X-ray diffraction. *Biophysical J.* **12**: 1285-1295. PMID: PMC1484226
40. Kirschner DA, Inouye H, Ganser AL, Mann V. (1989) Myelin membrane structure and composition correlated: a phylogenetic study. *J Neurochem* **53**: 1599–1609.

41. Kirschner DA, Blaurock AE. (1992) Organization, phylogenetic variations and dynamic transitions of myelin structure. In: R.E Martenson, ed. *Myelin: Biology and Chemistry*, Boca Raton: CRC Press. 3–78.
42. Quarles RH, Macklin WB, Morell P. (1999) Myelin Formation, Structure and Biochemistry. *In Basic Neurochemistry*, 6th ed., G. J. Siegel, , B. W. Agranoff, R. W. Albers, S. K. Fisher, and M. D. Uhler., editors. Lippincott-Raven publishing, Philadelphia. pp. 51-71.
43. Luo XY, Cerullo J, Dawli T, Priest C, Haddadin Z et al. (2008) Peripheral myelin of *Xenopus laevis*: Role of electrostatic and hydrophobic interactions in membrane compaction. *J. Struct. Bio.* **162**: 170-183. [doi:10.1016/j.jsb.2007.10.012](https://doi.org/10.1016/j.jsb.2007.10.012)
44. Inouye H, Kirschner DA. (1988) Membrane interactions in nerve myelin. II Determination of Surface Charge from Biochemical Data. *Biophys. J.* **53**: 247-260.
45. Vidal BdC, Mello MLS, Caseiro Filho AC, Godo C. (1980) Anisotropic properties of the myelin sheath. *Acta Histochem.* **66**: 32-39. <http://www.ncbi.nlm.nih.gov/pubmed/6776776>
46. Altamura M., Elvevag B., Campi G., De Salvia M., Marasco D., Ricci A., Bellomo A., (2012) Toward scale-free like behavior under increasing cognitive load, *Complexity*, **18**: 38-43 <http://onlinelibrary.wiley.com/doi/10.1002/cplx.21407/abstract> DOI: 10.1002/cplx.21407
47. Bianconi G, Marsili M (2006) Emergence of large cliques in random scale-free networks. *EPL (Europhysics Letters)*, **74**: 740-746. [doi:10.1209/epl/i2005-10574-3](https://doi.org/10.1209/epl/i2005-10574-3) <http://iopscience.iop.org/0295-5075/74/4/740>
48. Fratini M, Poccia N, Ricci A, Campi G, Burghammer M, Aeppli G, and Bianconi A Scale-free structural organization of oxygen interstitials in  $\text{La}_2\text{CuO}_{4+y}$  (2010) *Nature*, **466**: 841-844 Doi: 10.1038/nature09260
49. Ricci A., Poccia N., Campi G., et al. (2013) Multiscale distribution of oxygen puddles in 1/8 doped  $\text{YBa}_2\text{Cu}_3\text{O}_{6.67}$  *Scientific Reports*. **3**: 2383. [doi:10.1038/srep02383](https://doi.org/10.1038/srep02383)
50. Poccia N, Ricci A, Innocenti D, and Bianconi A. (2009) A possible mechanism for evading temperature quantum decoherence in living matter by Feshbach resonance. *Int. J. Mol. Scie.*, **10**: 2084-2106. <http://www.mdpi.com/1422-0067/10/5/2084> doi: 10.3390/ijms10052084.
51. Poccia N, Bianconi A (2011) The physics of life and quantum complex matter: a case of cross-fertilization *Life* **1**: 3-6. doi:10.3390/life1010003